Thyroid Nodule Segmentation and Component Analysis in Ultrasound Images

Chuan-Yu Chang*, Hsin-Cheng Huang*, and Shao-Jer Chen†
*Institute of Computer Science and Information Engineering,
National Yunlin University of Science & Technology, Yunlin, Taiwan
E-mail: chuanyu@yuntech.edu.tw
†Department of Radiology, Buddhist Dalin Tzu Chi General Hospital, Chia-Yi, Taiwan

***Abstract*— Heterogeneous thyroid nodules with distinct components are similar to background in ultrasound image. This results in a difficult task when radiologists and physicians manually delineate the complete shape of a nodule, or distinguish what kind of components it has. Hence, this paper presents an automatic process for nodule segmentation and component classification. A decision tree algorithm is used to segment the possible nodular area. A refinement process is then applied to recover the nodular shape. Finally, a hierarchical classification method based on support vector machine (SVM) is used to identify the components in the nodular lesion. Experimental results of the proposed approach were compared with those of other segmentation methods and showed a good performance.**

I. INTRODUCTION

Thyroid glands belong to the endocrine system. They are located in the neck just in front of the larynx. Thyroid nodules are common in adults and are indicative of potential thyroid cancer. The thyroid nodule rate is approximate 2-7% of the population in United States, Europe, and Japan [1].

Previous studies primarily focused on lesion classification with manual delineations of tumor boundaries. However, malignant tumors are often embedded the surrounding tissue. As a result, the boundary, which has fine linear strands extending irregularly outward from the main tumor, is obscured. In order to increase reliability and reduce the number of operations such as biopsy and fine needle aspiration, computer-aided diagnosis (CAD) is necessary [2].

Sonography is an alternative sensitive and convenient modality for initial evaluation and follow-up [3]. The advent of high resolution ultrasound (US) technology as a preoperative diagnostic tool has made possible the acquisition of detailed information and characteristics of the thyroid gland structure. However, poor US image quality and drawbacks caused by the nature of ultrasound limit the performance of various segmentation methods [1].

Decision trees can be constructed using many algorithms. Decision trees have several advantages in biomedical applications. They can be effectively used to classify any data structure, they can be used for prediction in non-linear problems, and they can effectively eliminate outliers [4].

Support vector machines (SVM) constitute a supervised learning technique rooted in Statistical Learning Theory developed by Vapnik *et al*. at AT&T Bell laboratories. SVM has gained popularity due to its many attractive advantages and promising empirical performance [5].

In this paper, an automatic thyroid nodule segmentation algorithm and a component classification method are proposed. The proposed method utilizes a decision-tree-based classifier for segmenting the nodular region. In order to obtain a more complete nodular shape, we refine the nodular shape using image processing technique. We then identify the components in the detected nodular area using a hierarchical SVM. The proposed method reduces the time required for radiologists to manually delineate and analyze nodular lesions. Experimental results show that the proposed method performs well.

The rest of this paper is organized as follows. Section II describes the preprocessing. Section III describes the segmentation algorithm. Section IV introduces nodular shape refinement. Section V introduces the classification. The experimental and comparison results are shown in Section VI. Finally, conclusion is given in Section VII.

II. PREPROCESSING

Figure 1 shows a flowchart of the proposed system. The objective of preprocessing is to enhance the contrast of the object (nodule) and background (non-nodule). The enhanced image is then used to segment the nodular region. Besides, some noise is hidden in US image, which results in a bad image quality. The noise is filtered out in the spatial domain by the direct manipulation of pixels in the image.

A. Image Enhancement

A histogram equalization method enhances the contrast between the nodule and background. This improvement is significant in results of the subsequent processes. A 3×3 median filter is applied to suppress speckle noise and to improves image quality.

B. Suspicious Nodular Area Detection

The method utilizes two bounds: horizontal projection and vertical projection, to locate the suspicious thyroid regions. This restricts the location of the segmentation and excludes some artifacts of the images. An example is shown in Fig.2. Anatomical information in the image is obtained and the

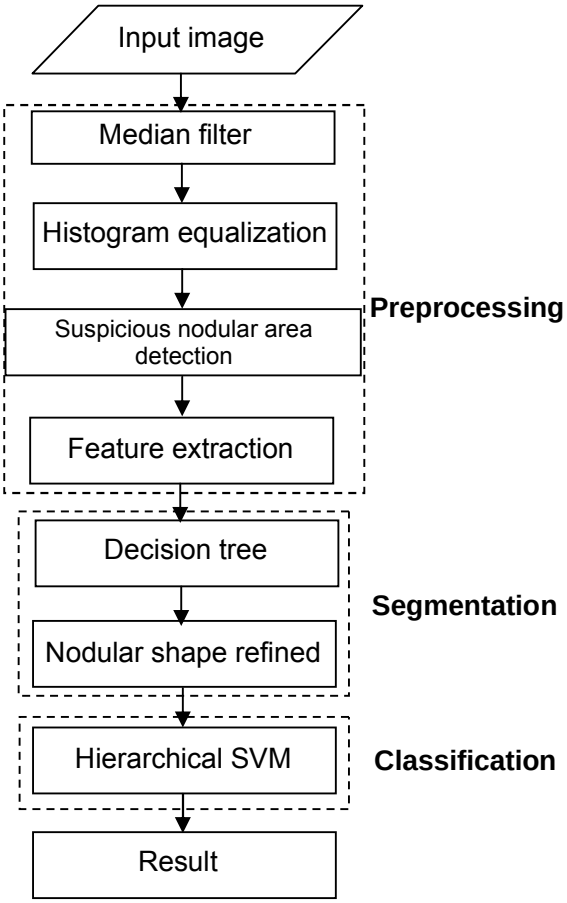

Fig. 1 Flowchart of the proposed system.

image is divided into three parts: skin, thyroid area, and dark region. Among of three parts, skin has higher gray levels, and the intensity of thyroid area is between skin and dark region.

According to the characteristics, a horizontal projection is utilized to separate the thyroid area from other parts. We calculate the average intensity for each row of the image. Then, we scan the image from bottom to top to find the first 15% average intensity, and mark the position of the value as T_t. In the same way, scanning the image from bottom to top receives a lower bound, T_b, which is the last 15% average intensity. Vertical projection is used to shrink the width of the nodule area. Without loss of generality, gray levels of non-nodules and artifacts are often higher and lower than thyroid nodule, respectively. Assume that the nodule is in the central region of the image, we compute the average intensity of each column within the range limited by T_b and T_t. We then find the maximum value and the minimum value of the histogram and mark the position as T_h or T_l, respectively.

C. *Feature Extraction*

We calculate 41 features from a block of $M \times M$ pixels. The sliding window method is used, for which blocks are arrayed adjacent to each other with an $M \times (M-1)$ overlap. The features are described briefly in the following:

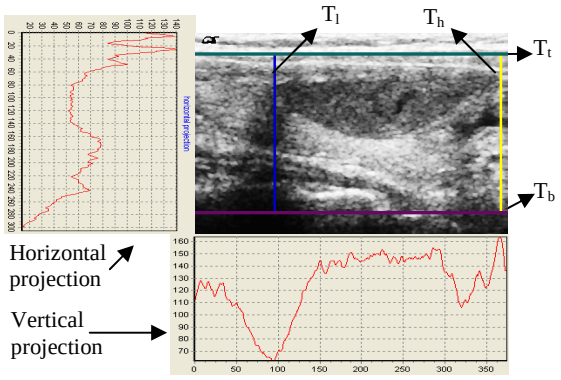

Fig. 2 Example of locating a suspicious nodule area.

1) *Co-occurrence Matrix:* The co-occurrence matrix was proposed by Haralick *et al.* [6]. It is a two dimensional array where rows and columns represent the gray level, respectively. 13 features are extracted from the co-occurrence matrix: **F1)** correlation, **F2)** difference entropy, **F3)** difference variance, **F4)** sum average, **F5**) sum entropy, **F6**) sum of squares, **F7**) sum variance, **F8**) contrast, **F9**) energy, **F10**) entropy, **F11**) local homogeneity, **F12**) cluster shade, and **F13**) cluster prominence.

2) *Statistical Feature Matrix:* The statistical feature matrix is a statistical analysis about the traits of distances between pixels as [7]:

$$Dissimilarity = \frac{\sum_{x=0}^{\Delta x-1}\sum_{y=0}^{\Delta y-1}\left(Dissimilarity\ Matrix(x,y)\right)}{\Delta x \Delta y} \quad (1)$$

$$Dissimilarity\ Matrix(\Delta x, \Delta y) = E\{|I(x,y) - I(x+\Delta x, y+\Delta y)|\} \quad (2)$$

where $I(x, y)$ denotes the gray-level value of a pixel at position (x, y) in an image I. $E\{\cdot\}$ denotes the expectation operation. Δx and Δy are user-specified inter-sample spacing distance. The **F14**) dissimilarity is obtained.

3) *Gray Level Run-Length Matrix:* The gray level run-length matrix is derived information from the relationship of distance and angle. Five features are calculated from the gray level run-length matrix [8]: **F15**) short runs emphasis, **F16**) long runs emphasis, **F17**) gray level uniformity, **F18**) run length uniformity and **F19**) run percentage.

4) *Laws' Texture Energy Measures:* This texture-energy approach uses three vectors: L3 = (1, 2, 1), E3 = (-1, 0, 1), and S3 = (-1, 2, -1) to measures the amount of variation within a fixed-size window [9]. L3, E3 and S3 vectors represent a center-weighted local averaging, the edges and the spots, respectively. Convoluting one vector with themselves or others we obtain three new vectors: L5 = L3 ∗ L3 = (1, 4, 6, 4, 1), E5 = L3 ∗ E3 = (-1, -2, 0, 2, 1), and S5 = L3 ∗ S3 = (-1, 0, 2, 0, -1), where ∗ represents a convolution operator. With further operation, we can generate five Laws' 5×5 masks: LE = $L5^T \times E5$, EL = $E5^T \times L5$, SL = $S5^T \times L5$, EE = $E5^T \times E5$, and LS = $L5^T \times S5$. The features computed from Laws' texture energy

measures include: **F20**) LE mean, **F21**) EL mean, **F22**) SL mean, **F23**) EE mean, **F24**) LS mean, **F25**) LE variance, **F26**) EL variance, **F27**) SL variance, **F28**) EE variance, and **F29**) LS variance.

5) *Neighboring Gray Level Dependence Matrix:* This is a two-dimensional matrix constructed by the gray level relationship between every pixel and its neighbors in an image [10]. The following features extracted from this matrix are: **F30**) small number emphasis, **F31**) large number emphasis, **F32**) number nonuniformity, **F33**) second moment and **F34**) entropy.
6) *Homogeneity:* The method is a major measurement for degree of smoothness. Let $h_{x,y}$ be a pixel located at (x,y). The equation is defined as:

$$h_{x,y} = \frac{\sqrt{\sigma_{x,y}} \times \sigma_{x,y}}{\mu_{x,y}} \tag{3}$$

where $\mu_{x,y}$ is local mean and $\sigma_{x,y}$ is local variance of a pixel located at (x,y) with a block size of $M \times M$. The feature is applied as **F35**) homogeneity feature.
7) *Histogram:* The value of histogram $HF_{x,y}$ is yielded using:

$$HF_{x,y} = \sum_{I=H-10, I\neq H}^{H+10} histo\ (I)$$
$$H = \arg\max_{I}(\ histo\ (I)) \tag{4}$$

where *histo(I)* is $M \times M$ block size histogram and I presents gray-level value. The feature is **F36**) histogram feature.
8) *Block Difference of Inverse Probability:* This feature [11] is evaluated difference between the number of pixels in a block and the ratio of the sum of pixel intensities in the block to the maximum in the block. That is

$$BDIP = M^2 - \frac{\sum_{(x,y)\in B} I(x,y)}{\max_{(x,y)\in B} I(x,y)} \tag{5}$$

where $I(x,y)$ is a gray level of a pixel and B means the size of $M \times M$ block. According the operation, **F37**) BDIP feature is attained.
9) *Discrete Cosine Transform (DCT)*: Rather than space domain, DCT is used to calculate variation of frequency of an image in frequency domain. Here we involved the lowest band in DCT coefficient as **F38**) DCT feature.
10) *Normalized Multi-scale Intensity Different:* This feature [12] mainly computes differences between pixels with vertical, horizontal, diagonal and asymmetric diagonal directions. The feature presents as **F39**) NMSID feature.
11) *Haar Wavelet*: The haar wavelet is a common and preferred method in frequency domain. It retrieves the characteristics by transforming information in spatial domain to frequency domain. So we utilize two features: **F40**) Mean of LL band **F41**) Variance of LL band.

III. SEGMENTATION ALGORITHM

Figure 3 shows a flow diagram of the decision-tree-based segmentation. The regions of interest (ROIs) were outlined by a physician and confirmed by biopsy. We extracted and discretized the features of nodules and non-nodules for use as a training set in the data preprocessing phase. Then we calculated the features to construct a model and used specific features for segmenting the US image. The result of a segmented nodule is a binary tree.

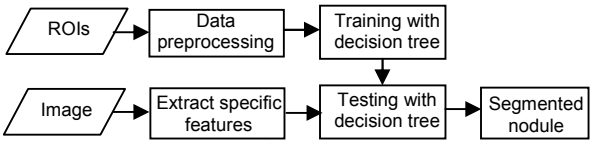

Fig. 3 Flow diagram for segmentation using a decision tree.

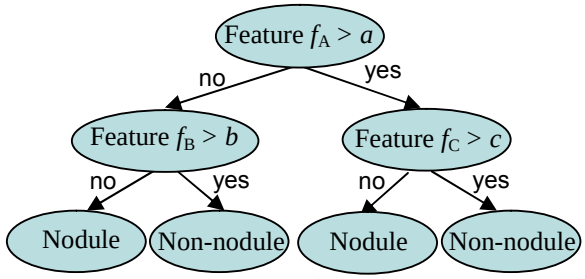

Fig. 4 Example of a decision tree.

A. Data Discretization

After extracting the features, we obtain the input vectors defined as:

$$X_i = [\, f_{i1}, f_{i2}, ..., f_{i41}\,] \quad i = 1,...,N \tag{6}$$

where X_i is the ith sample with the values of 41 features, N is total number of training data points.

The features are derived through Z-Score normalization [13], which normalizes each feature with mean and standard deviation as following:

$$f'_{ij} = \frac{f_{ij} - \overline{A_j}}{\sigma_{\overline{A}_j}} \qquad i = 1,...,N \tag{7}$$

where f_{ij} is the jth feature of the ith data point, f'_{ij} is transferred from f_{ij}, $\overline{A}_j$ and $\sigma_{\overline{A}_j}$ are the mean and standard deviation of the jth feature , respectively.

Because the normalization of features has continuous distributions, we use the equi-width binning method with ten intervals, whose length of each interval is defined as ($max\_ f'_j$ - $min\_ f'_j$) /10. In the formula $max\_ f'_j$ is the maximum value and $min\_ f'_j$ is the minimum value of the jth feature. The normalized values are then discretized into these intervals.

B. Decision Tree Model Concept

In the tree structure, each internal node (including the root) is associated with a feature. And a condition determined by the feature splits a branch node into two. The leaf nodes represent classification results of nodules or non-nodules in our method. An example is shown in Fig.4.

C. Specific Feature Evaluation with Gain Ratio

To construct the decision tree, we need to attain a feature corresponding to an internal node. The gain ratio is a measurement used for selecting the adequate feature [4]. Before evaluating the gain ratio, the entropy is calculated as:

$$Entropy(N) = -\sum_{r=1}^{C} p(N,r)\log_2 p(N,r) \quad (8)$$

where N is the training set, C is the number of the classes, $p(N,r)$ is the ratio that the number of the data of the rth class is consisted in N. Because there are two classes, nodule and non-nodule, we set C=2.

Based on the equation (8), for each feature we calculate the information gain using:

$$Gain(N, j) = Entropy(N) - \sum_{k=1}^{M} \frac{|N_k|}{|N|} Entropy(N_k) \quad j = 1,..,41 \quad (9)$$

where N_k is a subset of the training set N corresponding to the value k of the jth feature, $|N_k|$ is the number of subsets N_k, and M represents the total partitions of the jth feature. The derivation of $Entropy(N_k)$ is similar to that of (8).

In order to calculate the gain ratio, the $SplitInfo(N,j)$ is obtained using:

$$SplitInfo(N, j) = -\sum_{k=1}^{M} \frac{|N_k|}{|N|} \log_2 (\frac{|N_k|}{|N|}) \quad (10)$$

Finally, the ratio of information gain is calculated as:

$$GainRatio(N, j) = \frac{Gain(N, j)}{SplitInfo(N, j)} \quad (11)$$

We select the feature for internal nodes using:

$$\Gamma = \arg\max_j (GainRatio(N, j)) \quad (12)$$

The decision tree is constructed by maximizing the gain ratio Γ of the jth feature for partitioning.

D. Feature with Maximum Entropy Score

There may be more over than one feature for a particular gain ratio. To avoid this situation, entropy score obtains the optimal feature with the maximum entropy score for an internal node. The equation is as:

$$E(j) = \frac{1}{2}\left[\frac{(\sigma_j^{(+)})^2}{(\sigma_j^{(-)})^2} + \frac{(\sigma_j^{(-)})^2}{(\sigma_j^{(+)})^2} - 2 + (\bar{X}_j^{(+)} - \bar{X}_j^{(-)})^2 \left(\frac{1}{(\sigma_j^{(+)})^2} + \frac{1}{(\sigma_j^{(-)})^2}\right)\right] \quad (13)$$

where j is the jth feature, $\bar{X}_j^{(+)}$ and $\bar{X}_j^{(-)}$ are the averages of the jth feature of the nodule, and non-nodule samples. $\sigma_j^{(+)}$ and $\sigma_j^{(-)}$ are the standard deviations.

E. Pruning

A pre-pruning method is used to improve the complex tree model. It increases the tolerance for new data [14]. We use a pre-pruning method with two criteria: expected error and backed-up error. Expected error is defined as:

$$Expect\ Error\ (Node) = (\ N - n + k - 1\ ) / (N + k) \quad (14)$$

where *Node* is a current node to be evaluated, N presents samples in the current node, n is the number of N samples in the node that belongs to the majority class, and k is the number of classes.

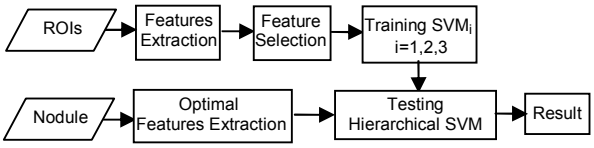

Fig. 5 Flowchart of classification.

Backed-up error is defined as:

$$Backed\text{-}up\ Error\ (Node) = P_1 \times Expect\_Error(Left\_Child\_Node) + P_2 \times Expect\_Error(Right\_Child\_Node) \quad (15)$$

where P_i $i=1,2$ are the weights of left child and right child of the current node *Node*, respectively.

If backed-up error is larger than expected error for a node, pruning is necessary to remove the children of the node for decreasing misclassification.

IV. Refining Shape of Nodular Area

The above procedures can be almost segment the thyroid region completely. However, there still existed some artifact may be classified as part of a nodule. A morphological technique is utilized to separate the artifacts from a nodule. Erosion with a 3×3 structuring element is derived to remove the connection between artifacts and nodules. In our experiment, 4-time erosion is effective to acquire adequate results. In order to remove artifacts near a nodule, a labeling process is applied [9]. The principle of the labeling technique is that many objects which are not connected together are marked with different labels to resent various objects. Hence, the nodule and artifacts are distinct objects to own label themselves and the object owning a larger number of labels is viewed as the nodule. In other words, small parts are regarded as artifacts and removed. Because the process of erosion shrinks the size of original nodule and made some "holes" in the nodule, two specific region growing stages are utilized to recover the shape of the nodule. One stage is the region filling [15], which fills "holes" in the nodule after erosion. The other stage is based on the convex hull concept [16], which uses four structuring elements to fill the shape of the nodule completely. If the structuring element mask matches the 3×3 region of the thyroid gland region, an action of filling is triggered. Through the procedure, the final contour of nodule shape is delineated smoother and similar to the status of original one.

V. The Classification Method

We now need to understand the components hiding in the nodule. Support vector machine (SVM), a popular and robust classifier, is utilized for our experiment. The training set is collected from the ROIs of four components outlined by radiologist and confirmed by biopsy. Fig. 5 shows a flowchart of the hierarchical SVM, which combines with three binary-SVMs. Each one probes different characteristics and elements in the segmented nodule.

A. Feature Selection

Because there are a large number of features to analyze the thyroid nodule, a powerful feature selection for reducing features and increasing accuracy of classification is required [17]. First, given normalized vectors $\boldsymbol{V}_i$, $i=1,\ldots, N$, where N is total number of feature vectors. Then calculate F-score defined:

$$Fscore(j)=\frac{(\bar{v}_j^{(+)}-\bar{v}_j)^2+(\bar{v}_j^{(-)}-\bar{v}_j)^2}{\frac{1}{n_+-1}\sum_{i=1}^{n_+}(v_{ij}^{(+)}-\bar{v}_j^{(+)})^2+\frac{1}{n_--1}\sum_{i=1}^{n_-}(v_{ij}^{(-)}-\bar{v}_j^{(-)})^2} \quad (16)$$

where $\bar{v}_j$, $\bar{v}_j^{(+)}$ and $\bar{v}_j^{(-)}$ are the average of the jth feature of the whole, positive, and negative data sets, respectively. $v_{ij}^{(-)}$ is the jth feature of the ith negative instance, $v_{ij}^{(+)}$ is the jth feature of the ith positive instance, n_+ and n_- are number of positive and negative instances such as follicle and fobrosis base, respectively.

The SVM classifier generates a hyperplane which separates two classes using the equation as follows [3]:

$$g(V)=sign\left(\sum_{i=1}^{N}\alpha_i d_i k(V_i^T V)+b\right) \quad (17)$$

where α_i represents weight parameters, $k(V_i^T V)$ is the kernel function, V_i is the input pattern of the ith example, V is the input vector, $d_i \in \{1,-1\}$ is the desired output, and b is the bias.

A 3-fold cross validation-SVM is then used to evaluate the performance of dissimilar combination with the features. In this paper, we utilize libsvm [18] to implement the SVMs.

B. Hierarchical SVM

Figure 6 shows the structure of the hierarchical classifier. Four components in a nodule**,** enlarged follicles, cells with follicles, fibrosis and cells with fibrosis are detected by three SVMs — **SVM1, SVM2** and **SVM3** which composed the hierarchical SVM.

Trained **SVM1** is constructed to separate the follicle base and fibrosis base. We extract the optimal features using $M\times M$ blocks from the US image as testing data for **SVM1**. Here we denote the result of follicles base as +1, and that of fibrosis base as -1. In order to locate the address of region of the nodule, we use a functional map which records the labels of the nodule. Each label corresponds to a coordinate of the image f(x, y). We then form a reference map for the next step to analyze components of the nodule. In the next stage, for further analyze the elements of the nodule, **SVM2** predicts the results and we use +1 for enlarged follicles and -1 for cells with follicles. Similarly, **SVM3** discriminates between fibrosis (+1) and cells with fibrosis (-1).

VI. EXPERIMENTAL RESULTS

The source of US images with 256 gray levels pixels and 300×360 pixels in size, were supplied by the radiologist in the Department of Radiology, Buddhist Dalin Tzu Chi General Hospital. From January 2005 to March 2007, 61 patients (48 females and 13 males, age range: 23-82 years old) with 76 thyroid nodular lesions were studied. Furthermore, there were 324 ROIs of non-nodules obtained, 59 ROIs of enlarge follicles, 141 ROIs of follicle base, 57 ROIs of cells with fibrosis and 50 ROIs of fibrosis. The software development environment was Builder 6.0, Matlab 7.1 and Python 2.5 on an Intel Pentium IV 2.8 GHz processor with 1GB of RAM; moreover, we selected the RBF kernel of libsvm, which is defined as [19]:

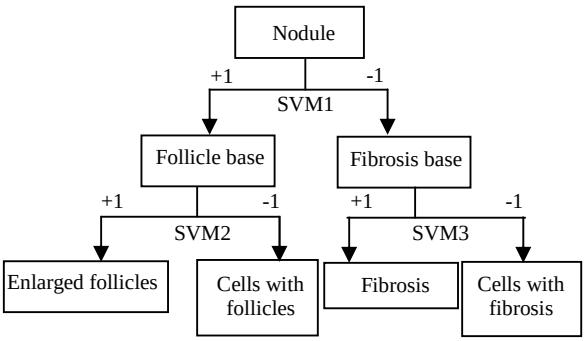

Fig. 6 Architecture of hierarchical SVM for four components.

$$\exp\left(-\frac{1}{2\sigma^2}\|V-V_i\|\right)^2 \quad (18)$$

where σ^2 is the width of the kernel.

The proposed method was compared with well-known methods such as region growing algorithm [20] and fuzzy c-means clustering algorithm [21]. For region growing algorithm, the position of the seed point and the criterion of absolute difference between any pixel and its 8-adjacency pixels were two significant parameters taken into account. These parameters which obtained the most reasonable result were applied by trial-and-error. In fuzzy c-means clustering algorithm, the initial number of the clusters was 2. Fig. 7(a)—(c) illustrate the contours of three distinct nodules manually delineated by the radiologist. Fig. 7(d)—(f) show the detected suspicious thyroid nodule area.

Because the more complete the prototype of nodule was obtained, the easier shape refinement of the nodule recovered afterwards. Based on the idea, Fig. 7(g) — (i) show the segmentation results of the proposed segmentation algorithm before refining shape within the area in Fig. 7(d)—(f). Fig.7(j) —(l) show the results of the region growing algorithm, which presented slightly fragmental shapes of the nodules. Fig. 7(m) —(o) show the segmented results of fuzzy c-means clustering algorithm, and the results had an over-sensitive phenomenon that more pixels of non-nodule were clustered as nodule. Compare the proposed method with region growing algorithm and fuzzy c-means clustering algorithm, the latters obtained fragmental appearance. Moreover, the proposed method gained a proper result with automatic process than semi-automatic process of the region growing algorithm. We also compared k-nearest neighbor (KNN) classifier and disk expansion (DE) segmentation method [2] with our proposed

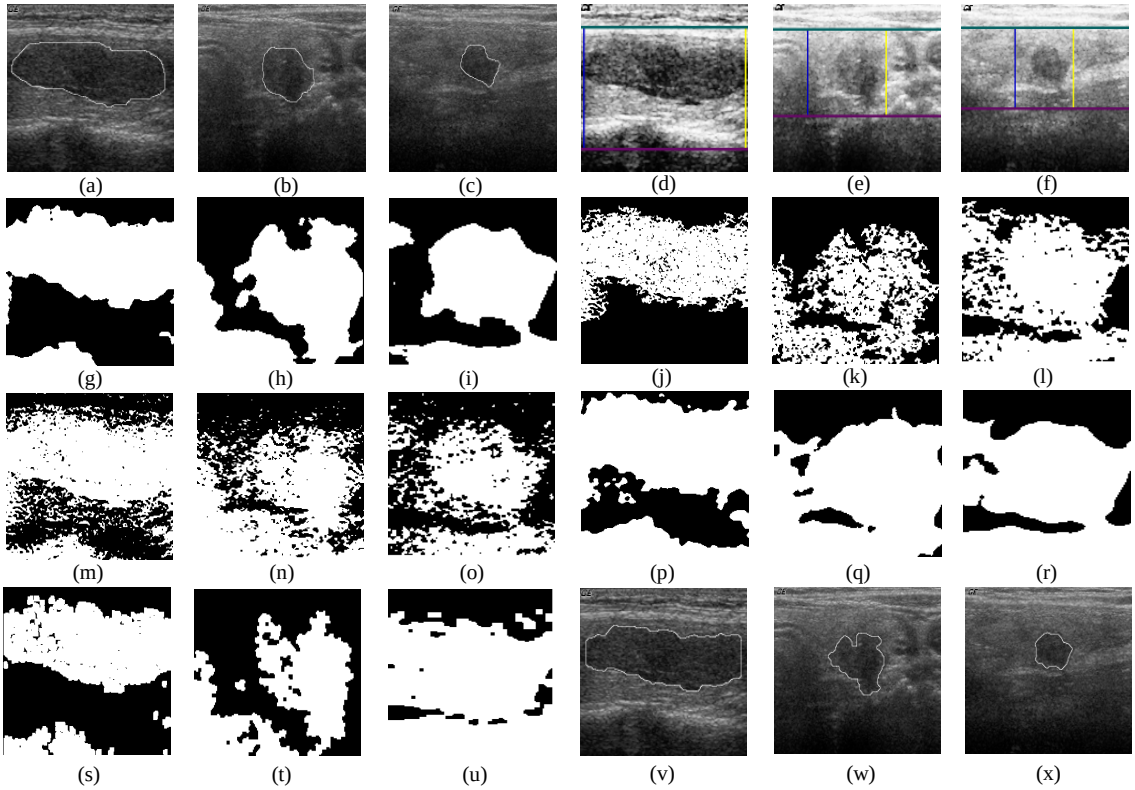

Fig. 7 (a) —(c) Manual delineation of three nodules. (d) —(f) Suspicious nodular area from (a) —(c). (g) —(i) The proposed method without refinement.(j) —(l) Region growing. (m) —(o) FCM. (p) —(r) KNN. (s) —(u) DE scheme. (v) —(x) Final contours of the segmentation using our method.

method. Here we used the parameter k=3 as 3-NN and the results are shown in Fig. 7(p)—(r). Fig. 7(s)—(u) show the results of DE scheme which were set the percent p = 70% empirically at first round. In order to derive an appropriate result, the DE segmentation performed dilation following erosion two times to eliminate some small holes. The results presented that the boundaries were not smooth enough because adaptive thresholding was retarded in uneven gray levels of boundaries. Fig. 7(v)—(x) show the results of the proposed method after nodular shape refinement.

The semi-automatic segmentation algorithm active contour model (ACM) [22] and the watershed segmentation algorithm [15] were compared with the proposed method. These two methods were implemented with Open Source Computer Vision Library (OpenCV), a popular image processing library, to assist us in deriving the results. For ACM, two parameters can be adjusted: internal forces and external forces, which controlled the curve compactness and the motion toward the curve borders, respectively. Additionally, an initial contour is given for delineating the nodule. The watershed segmentation algorithm is subject to set the initial internal marker associated with objects in interest and external marker associated with the background. The accuracy of the results depends on the initial contours, so the stability is easily affected by users' initial selection.

Figures 8(a)—(c) show the manual contours of three representative nodules. Fig. 8(d)—(f) are the results of ACM, the yellow line is the initial contour given by user. And the green line is the result of ACM. The initial internal and external markers of the watershed algorithm obtained using manual delineation are shown in Fig. 8(g)—(i). The results of the watershed algorithm are shown in Fig. 8(j)—(l). Figures 8(m)—(o) show the detection results for the proposed method.

To evaluate the capability of the proposed method, the corresponding performances of our method, ACM and watershed algorithm in Fig. 8 were measured. Five measures, including accuracy, sensitivity, specificity, negative predictive value (NPV), and positive predictive value (PPV) were calculated. Each equation is defined as:

$$Accuracy = \frac{N_{tp} + N_{tn}}{N_p + N_n} \tag{19}$$

$$Seneitivit\ y = \frac{N_{tp}}{N_p} \tag{20}$$

$$Specificit\ y = \frac{N_{tn}}{N_n} \tag{21}$$

$$NPV = \frac{N_{tn}}{N_{tn} + N_{fn}} \tag{22}$$

$$PPV = \frac{N_{tp}}{N_{tp} + N_{fp}} \tag{23}$$

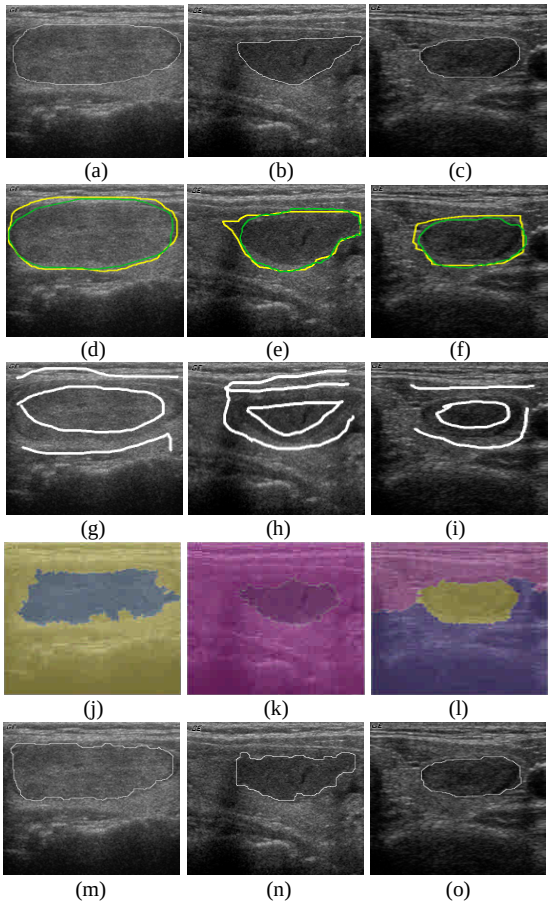

Fig. 8 (a)－(c) Manual delineation. (d)－(f) ACM results. (g)－(i) Internal and external markers of watershed. (j)－(l) Results for the watershed algorithm. (m)－(o) Results for proposed method.

where we let N_p be the total number of nodular pixels and N_n denotes the total number of non-nodular pixels. N_{tp} is the number of pixels in the actual nodule and detected by the proposed method and N_{fp} is the number of pixels detected as a nodule but actually part of the normal tissue. Hence, the true negative pixels N_{tn} and false negative N_{fn} can be defined as $N_{tn} = N_n - N_{fp}$ and $N_{fn} = N_p - N_{tp}$, respectively.

Table 1 shows the performance of the proposed method. Table 2 and Table 3 are performances of the ACM and the watershed algorithm, respectively. We discovered our method presented higher average performances than the others. And the performances of the proposed method obtained from five measures of each case were all larger than 80%. This meant our method had capable of stability.

Furthermore, Fig. 9(a)－(c) show the classification results of four components in three representative nodules from original images in Fig. 8(a)－(c). The corresponding colors of the four components are depicted in Table 4.

To show that the feature selection method can attain the optimal features, the scatter distributions using SVM classifier are shown in Fig. 10. Fig. 10(a) shows a feature space of two

Table 1. The performance of the proposed method

	Accuracy	Sensitivity	Specificity	NPV	PPV
Case 1	96.4%	91.0%	98.9%	96.0%	97.3%
Case 2	97.8%	93.5%	98.4%	99.0%	90.4%
Case 3	98.8%	96.3%	99.1%	99.5%	93.5%
Case 4	96.4%	93.8%	97.2%	97.9%	92.0%
Case 5	97.3%	82.9%	98.4%	98.6%	80.2%
Case 6	98.6%	80.3%	99.3%	99.2%	81.7%
Average	97.5%	89.6 %	98.5%	98.3%	89.1%

Table 2. The performance of ACM

	Accuracy	Sensitivity	Specificity	NPV	PPV
Case 1	94.8%	95.9%	94.3%	98.1%	88.4%
Case 2	81.3%	58.2%	85.0%	93.0%	37.1%
Case 3	83.4%	47.7%	88.1%	92.7%	34.8%
Case 4	93.2%	99.9%	91.0%	99.9%	78.9%
Case 5	96.0%	99.5%	95.7%	99.9%	64.6%
Case 6	98.2%	94.7%	98.3%	99.8%	67.8%
Average	91.1%	82.6%	92.0%	97.2%	61.9%

Table 3. The performance of the watershed algorithm

	Accuracy	Sensitivity	Specificity	NPV	PPV
Case 1	89.2%	70.3%	97.8%	88.0%	93.4%
Case 2	94.8%	72.0%	98.3%	96.0%	87.0%
Case 3	95.3%	83.4%	97.0%	98.5%	78.2%
Case 4	89.0%	79.4%	92.3%	92.8%	78.3%
Case 5	96.7%	79.2%	98.1%	98.3%	76.8%
Case 6	97.6%	85.9%	98.0%	99.7%	62.0%
Average	93.7%	78.3 %	96.9 %	95.5 %	79.2 %

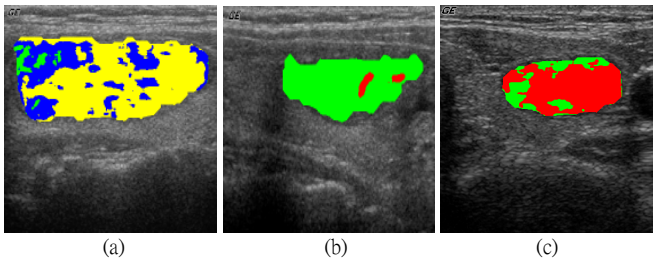

Fig. 9. (a)－(c) Distributions of components in three nodule from Fig. 8.

Table 4. Four components and their corresponding colors

Component Description	Color used
Enlarged follicle	Yellow
Cells with follicles	Blue
Fibrosis	Red
Cells with fibrosis	Green

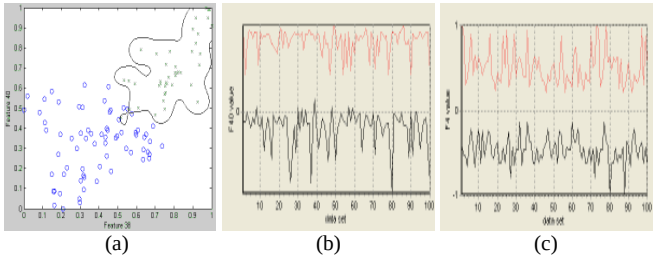

Fig. 10. Effectiveness of the selected features for classification. (a) F38 and F40 classify follicle base and fibrosis base, (b) F40 divides follicle base and fibrosis base, and (c) F4 separates fibrosis from cells with fibrosis of SVM1, SVM2 and SVM3, respectively.

dimensions associated with a hyperplane. In Fig. 10(b) and Fig. 10 (c), the x-axis and the y-axis present the training set and the output of SVM classifier with the optimal feature, respectively. Fig. 10(a) shows that **F38**) DCT feature and **F40**) Mean of LL-band divided follicle base and fibrosis base. Fig. 10(b) shows **F40**) Mean of LL-band was the optimal feature for separating enlarged follicles and cells with follicles in SVM2. Finally, Fig. 10(c) shows **F4**) Sum average of co-occurrence matrix was an excellent feature for classifying fibrosis and cells with fibrosis in SVM3.

VII. CONCLUSION

Ultrasound imaging is widely used to inspect the thyroid gland. However, similar gray levels between thyroid nodule and non-nodule can confuse the experts. In addition, artifacts also degrade the quality of US images making the real shape and the components of the nodules difficult to determine easily. To solve these problems, this paper presents an automatic method for segmenting nodules and classifying the components in the nodules. We develop a decision tree to segment the nodular area, and a shape refinement process is then applied to obtain a complete nodular contour. Finally, a hierarchical SVM classifier consisting of three SVMs is applied to analyze the components of a thyroid nodule. Experimental results show that the proposed method achieve high accuracy than other segmentation algorithm. In the future, the proposed method will be utilized to classify more components of nodules rather then four. Additionally, too many morphological operations should be avoided. The extended idea of our proposed method will persist to derive a delicate probe and large samples will be essential to valid the process.

ACKNOWLEDGMENT

This work was supported by the National Science Council, Taiwan, under grant NSC 96-2221-E-224-070. The author would like to thank the Department of Radiology, Buddhist Dalin Tzu Chi General Hospital, Chia-Yi, Taiwan, R.O.C., for support and guidance.

REFERENCES

[1] S. Tsantis, N. Dimitropoulos, D. Cavouras and G. Nikiforidis, "A hybrid multi-scale model for thyroid nodule boundary detection on ultrasound images," *Computer Method and Program in Biomedicine*, vol. 84, pp. 86-98, 2006.

[2] C. K. Yeh, Y. S. Chen, W. C. Fan and Y. Y. Liao, "A disk expansion segmentation method for ultrasonic breast lesions," *Pattern recognition*, vol. 42, pp. 596-606, 2009.

[3] S. J. Chen, S. N. Yu, J. E. Tzeng, Y. T. Chen, K. Y. Chang, K. S. Cheng, F. T. Hsiao and C. K. Wei, "Characterization of the major histopathological components of thyroid nodules using sonographic texture features for clinical diagnosis and management," *Ultrasound in Med. & Biol.*, vol. 35, no.2 , pp. 201-208, 2008.

[4] W. H. Chao, Y. Y. Chen, C. W. Cho, S.H. Lin, Y.Y. I. Shih and S. Tsang, "Improving segmentation accuracy for magnetic resonance imaging using a boosted decision tree," *Journal of Neuroscience Methods*, vol. 175, pp. 206-217, 2008.

[5] I. Maglogiannis, H. Sarimveis, CT. Kiranoudis, AA. Chatziioannou, N. Oikonomou and V. Aidinis, "Radial basis function neural networks classification for the recognition of idiopathic pulmonary fibrosis in microscopic images," *IEEE Trans. Inf. Technol. Biomed.*, vol. 12, No. 1, pp. 42-54, 2008.

[6] R. M. Haralick, K. Shanugam and I. Dinstein, "Textural features for image classification," *IEEE Trans. Sys., Man and Cyb.*, vol. 3, pp. 610-621, 1973.

[7] C. M. Wu and Y. C. Chen, "Statistical feature matrix for texture analysis", *CVGIP: Graphical Models and Image Processing*, Vol. 54, No. 5, pp. 407-419, 1992.

[8] M. M. Galloway, "Texture analysis using gray run lengths", *Computer Graphics and Image Processing*, vol. 4, pp. 172-179, 1975.

[9] L. G. Shapiro and G. C. Stockman, *Computer Vision*, Prentice Hall, 2001.

[10] C. J. Sun and W. G. Wee, "Neighboring gray level dependence matrix for texture classification", *Computer Vision, Graphics, and Image Processing*, vol. 23, no. 3, pp. 341-352, 1983.

[11] Y. D. Chum, S. Y. Seo, "Image retrieval using BDIP and BVLC moments," *IEEE Trans. Cir. & Sys. for Video Tech.*, vol. 13, no. 9, pp. 951-957, 2003.

[12] E. L. Chen, P. C. Chung, C. L. Chen, H. M. Tsai, C. I. Chang, "An automatic diagnostic system for CT liver image classification," *IEEE Trans. Biol. Eng.*, vol. 45, no. 6, pp. 783-794, 1998.

[13] S. Dua, H. Singh and H. W. Thompson, "Associative classification of mammograms using weighted rules," *Expert system with application*, vol.36, issue 5, pp.9250 – 9259, 2009.

[14] Quinlan, J. R., *C4.5: Programs for Machine Learning*, Morgan Kaufmann Publishers, 1993.

[15] R. C. Gonzalez and R. E. Woods, *Digital Image Processing*, 2nd ed., Prentice-Hall International Edit, 2002.

[16] C. Y. Chang, Y.F. Lei, "Thyroid segmentation and volume estimation in Ultrasound images," *Proc. of the IEEE Conf. on Sys., Man and Cyb.*, pp. 3442-3447, 2008.

[17] C. Y. Chang, M. F. Tsai and S. J. Chen, "Classification of the thyroid nodules using support vector machines," *Proc. of the IEEE Inter. Join. Conf. on Neural Network*, pp.3093-3098, 2008.

[18] C. C. Chang and C. J. Lin, LIBSVM: a library for support vector machines, 2001. Software available at http://www.csie.ntu.edu.tw/~cjlin/libsvm.

[19] S. Haykin, *Neural Networks*, Prentice-Hall, Upper Saddle River, 1998.

[20] J. Dehmeshki, H. Amin, M. Valdivieso, and X. Ye, "Segmentation of pulmonary nodules in thoracic CT scans: a region growing approach," *IEEE Trans. Med. Imag.*, vol. 27, no.4, pp.467-480, 2008.

[21] S. Shen, W. Sandham, M. Granat, and A. Sterr, "MRI fuzzy segmentation of brain tissue using neighborhood attraction with neural-network optimization," *IEEE Trans. BIOM.*, vol. 9, no.3, pp.459-467, 2005.

[22] M. Kass, A. Witkin and D. Terzopoulos, "Snake: active contour model," *International Journal of Computer Vision*, pp.321 – 331, 1987.